Global ocean dimethylsulfide photolysis rates quantified with a spectrally and vertically resolved model

This article is a non-peer reviewed preprint. It was submitted to Limnology and Oceanography Letters for review on 21 October 2022

Martí Galí[1]*, Emmanuel Devred[2], Gonzalo L. Pérez[3], David J. Kieber[4], Rafel Simó[1]

[1]Institut de Ciències del Mar, CSIC, Passeig Marítim de la Barceloneta 37-49, 08003 Barcelona, Catalonia, Spain

[2]Fisheries and Oceans Canada, Bedford Institute of Oceanography, Dartmouth, NS B2Y 4A2, Canada

[3]Instituto INIBIOMA (CRUB Comahue, CONICET), Quintral 1250, 8400 S.C. de Bariloche, Rio Negro, Argentina

[4] Department of Chemistry, State University of New York, College of Environmental Science and Forestry, 1 Forestry Drive, Syracuse, New York 13210, United States

* Corresponding author: mgali@icm.csic.es

Keywords: DMS; UV radiation; photolysis; remote sensing; photochemical model; CDOM; photosensitizer; ocean.

Data availability statement: Data and code are available in https://doi.org/10.5281/zenodo.7204133.

Author contributions: M.G. conceived the study with initial contributions from R.S. and D.J.K. M.G. coded the photolysis model and ran the radiative transfer and photolysis calculations, processed the input and output datasets, made the figures and wrote the first draft of the manuscript. E.D. and G.L.P. contributed to underwater irradiance modelling. All authors commented on manuscript drafts and contributed to the final version.

Abstract

Photochemical reactions initiated by ultraviolet (UV) radiation remove the climate-active gas dimethylsulfide (DMS) from the ocean's surface layer. Here we quantified DMS photolysis using a satellite-based model that accounts for spectral irradiance attenuation in the water column, its absorption by chromophoric dissolved organic matter (CDOM), and the apparent quantum yields (AQYs) with which absorbed photons photodegrade DMS. Models with two alternative parameterizations for AQY estimate global DMS photolysis at between 17 and 20 Tg S yr^{-1}, equivalent to 13–15 Tg C yr^{-1}, of which ~73% occurs in the Southern hemisphere. This asymmetry results mostly from the high AQYs found south of 40°S, which more than counteract the prevailing low irradiance and deep mixing in that region. Simplified schemes currently used in biogeochemical models, whereby photolysis is proportional to visible radiation, likely overestimate DMS photolysis by around 150% globally. We propose relevant corrections and simple adjustments to those models.

Scientific Significance Statement

Dimethylsulfide (DMS) is a gas produced by marine microbes that, once emitted to the atmosphere, affects the formation of atmospheric particles (aerosols) and clouds, and hence climate. Several processes can remove DMS from the upper ocean layer, therefore controlling DMS emissions. One such process that has not been accurately quantified hitherto is the oxidation of DMS by chemical reactions initiated mostly by UV radiation. Using a model that combines satellite observations and in situ data, here we show that DMS photolysis varies across regions and seasons; and quantify global photochemical DMS removal from the surface ocean at around 20 million tonnes of sulfur per year, 30% less than DMS emission to the atmosphere. Our best estimates are not compatible with estimates from simplified equations for DMS photolysis that are currently used in the numerical models that inform climate projections, stressing the need to improve those models.

Introduction

The biogenic gas dimethylsulfide (DMS), produced mostly by pelagic microbial food webs, represents the largest natural source of atmospheric sulfur (Hulswar et al. 2022). The products of atmospheric DMS oxidation, chiefly methanesulfonic and sulfuric acids, promote new particle formation and growth, which overall results in planetary cooling through enhanced aerosol light scattering and cloud albedo (Shaw 1983; Charlson et al. 1987; Carslaw et al. 2013). Despite continued efforts to represent DMS-mediated feedbacks in Earth System models, these models do not accurately represent sea-surface DMS concentration fields (Tesdal et al. 2016) and cannot reliably predict future DMS emission trends under global change scenarios (Bock et al. 2021).

DMS is lost from the upper ocean mainly through bacterial and photochemical oxidation and ventilation to the atmosphere (del Valle et al. 2007, 2009; Galí and Simó 2015). Biogeochemical models must capture the variability in these processes to accurately reproduce sea-surface DMS concentration fields, which in turn largely control DMS emissions (Tesdal et al. 2016). However, large uncertainties in spatiotemporal DMS distribution remain owing to sparse observations, limited mechanistic understanding and insufficiently validated parameterizations (Le Clainche et al. 2010; Galí and Simó 2015).

Photochemical DMS removal is a photosensitized process, whereby DMS is oxidized by the reactive species generated through the absorption of solar radiation by optically active substances (Brimblecombe and Shooter 1986), mainly CDOM (Toole et al. 2003, 2004; Bouillon and Miller 2004; Galí et al. 2016). To quantify the efficiency of this process, an apparent quantum yield (AQY) is computed as the mol DMS oxidized per mol quanta absorbed by CDOM at each wavelength (λ). Typically, AQY decreases exponentially over the solar spectrum. Like other photochemical processes (Fichot and Miller 2010), the spectral product of AQY, CDOM absorption and irradiance produces a peak in DMS photolysis between 320–330 nm at the sea surface. The photolysis spectrum progressively shifts towards longer wavelengths as radiation propagates down the water column because shortwave UV attenuates faster than longwave UV and visible light. Thus, adequate spectral and vertical resolution are needed for accurate photochemical

modeling. Although this has been known for decades, DMS photolysis is still expressed as a function of visible light in biogeochemical models (Chu et al. 2003; Vogt et al. 2010; Belviso et al. 2012).

A global meta-analysis of in situ rates (Galí et al. 2016) found that variability in DMS photolysis AQY at 330 nm, AQY(330), was to first order an inverse function of the corresponding CDOM absorption coefficient, $a_{CDOM}(330)$ (Fig. 1). Smaller fractions of variance were explained by nitrate and temperature, which were nevertheless unable to account for the three orders of magnitude spanned by AQY(330) globally. Hence, it was concluded that CDOM composition mainly controlled AQYs through yet unknown processes. Building on this work, we implemented in the current study a spectrally and vertically resolved model that uses remotely sensed data to compute DMS photolysis rates in the global ocean and their spatiotemporal patterns. We compared our results to those obtained with two simple parameterizations extracted from prognostic biogeochemical models.

2. Model description and implementation

2.1 Empirical AQY models

Our spectrally resolved model relies on the empirical estimation of the DMS photolysis AQY at 330 nm and subsequently the AQY spectrum, AQY(λ) (units of s^{-1} [mol photons m^{-3} s^{-1}]$^{-1}$ = m^3 [mol photons]$^{-1}$). In the dataset compiled by Galí et al. (2016), AQY(330) data were fitted using two multiple regression models. The first model (*CDOM_NO3*) represents AQY(330) as a function of $a_{CDOM}(330)$ and nitrate concentration [NO_3^-]:

$$\log_{10}[AQY(330)] = -0.4548 - 0.8392 \cdot \log_{10}[a_{CDOM}(330)] + 0.0293[NO_3^-] \quad \text{eq. 1A}$$

The second model (*CDOM_SST*) represents AQY(330) as a function of $a_{CDOM}(330)$ and sea-surface temperature (SST), with a linear interaction term:

$$\log_{10}[AQY(330)] = -0.4629 - 1.5774 \cdot \log_{10}[a_{CDOM}(330)] + 0.0049 \cdot SST + \\ +0.0374 \cdot \log_{10}[a_{CDOM}(330)] \cdot SST \quad \text{eq. 1B}$$

Models *CDOM_NO3* and *CDOM_SST* accounted, respectively, for 84% and 83% of the $\log_{10}$-space variance of AQY(330) in the Galí et al. (2016) dataset (n = 111). The two models also had similar dispersion and bias (Fig. 1 and S1) and are therefore used in subsequent calculations (section 2.2). Following Galí et al. (2016), the AQY spectrum was computed from AQY(330) and a spectral slope S_{AQY} such that:

$$AQY(\lambda) = AQY(330)\cdot\exp[S_{AQY}\cdot(\lambda - 330)] \quad \text{eq. 2}$$

where S_{AQY} was itself a function of AQY(330) according to a fit that accounted for 29% of its observed variance (n = 47):

$$S_{AQY} = 0.0429 + 0.0147\cdot\log_{10}[AQY(330)] \quad \text{eq. 3}$$

2.2 Depth-dependent spectrally resolved model

Vertical profiles of the DMS photolysis rate constant, $k_{p,z}$ (d^{-1}), were computed as:

$$k_{p,z} = \int E_{d,0-}(\lambda)\cdot\exp(-K_d(\lambda)\cdot z)\cdot(1/\mu_d)\cdot a_{CDOM}(\lambda)\cdot AQY(\lambda)\, d\lambda \quad \text{eq. 4}$$

where $E_{d,0-}(\lambda)$ is the downwelling spectral irradiance just below the sea surface (mol photons m^{-2} d^{-1} nm^{-1}), $K_d(\lambda)$ is the diffuse vertical attenuation coefficient of downwelling irradiance (m^{-1}), μ_d is the mean cosine of underwater irradiance (required to convert planar irradiance to scalar irradiance; unitless), and $a_{CDOM}(\lambda)$ is the CDOM absorption coefficient spectrum (m^{-1}). The spectral terms in eq. 4 were computed at 5 nm resolution; spectral integration between 290 and 500 nm yielded the photolysis rate constant at a given depth. The vertical resolution decreased exponentially from 0.01 m at the surface to 20 m at 100 m (39^{th} vertical bin). The bottom level was determined by the mixed layer depth (MLD; obtained from Schmidtko et al. (2013)). Mean daily photolysis rate constants in the upper mixed layer, $k_{p,ML}$ (d^{-1}), were computed through trapezoidal integration of $k_{p,z}$ over time (3h intervals) and depth, followed by division by the MLD.

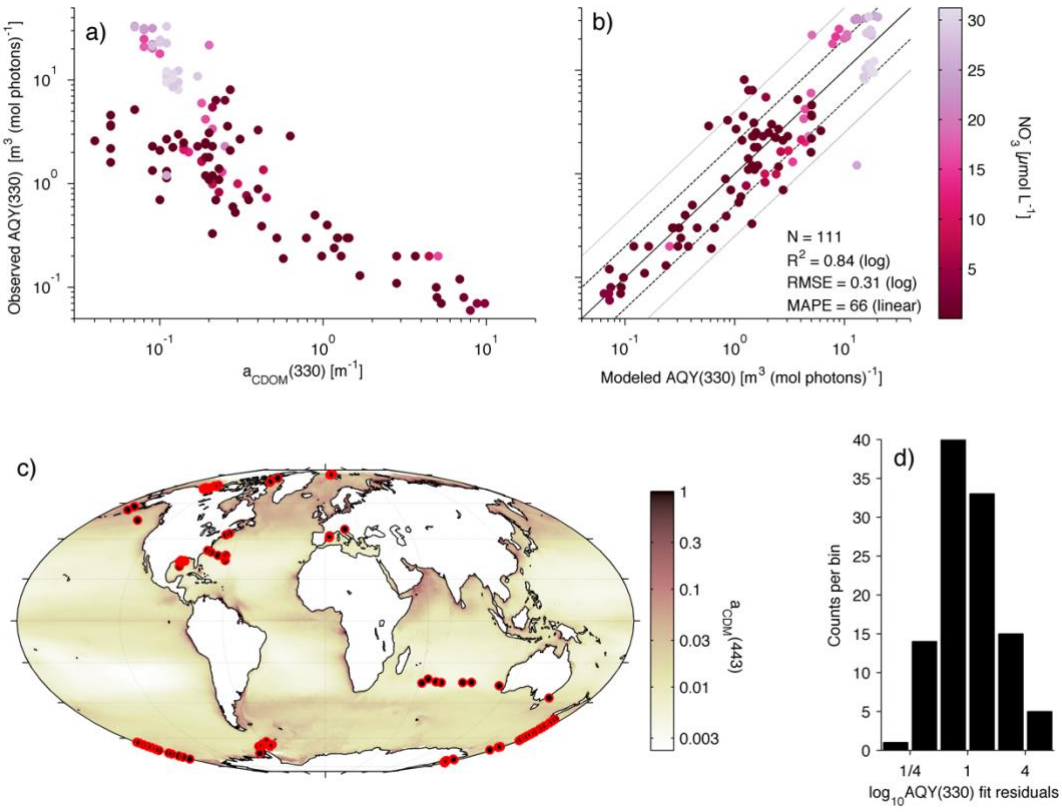

Figure 1. *(a) Relationship between apparent quantum yield at 330 nm, AQY(330), and the CDOM absorption coefficient, $a_{CDOM}(330)$; (b) comparison between observed AQY(330) and that predicted with an empirical model that uses $a_{CDOM}(330)$ and nitrate as predictors (eq. 1A); (c) map of the sampling locations overlaid on SeaWiFS-retrieved absorption of chomophoric detrital matter at 443 nm, $a_{CDM}(443)$, used to estimate $a_{CDOM}(330)$ in our model; (d) fit residuals. The color scale in a) and b) shows nitrate concentration. The black line in b) shows 1:1 model:data agreement, and the dashed and dotted lines show, respectively, deviations by a factor of 2 and 4 from the 1:1 line.*

Global $k_{p,z}$ fields were computed at 1°x1° horizontal resolution (Fig. 2), to which all input variables had been previously regridded. Mixed-layer photolysis rates, P_{ML} (nmol L^{-1} d^{-1}), were computed as the product of monthly 1°x1° fields of $k_{p,ML}$ and sea-surface DMS concentration (nmol L^{-1}) (Hulswar et al. 2022), assuming constant DMS in the upper mixed layer (UML). Gridded P_{ML} fields were finally integrated over different spatiotemporal domains (Table 1).

Detailed information on the input data and the optical sub-models used to compute the factors in eq. 4 and generate the associated intermediate datasets is provided in the Supplemental Material (SM1-3). Briefly, a global monthly climatology of $E_{d,0-}(\lambda)$ at 3h sub-daily resolution was computed using the atmospheric radiative transfer code SBDART (Ricchiazzi et al. 1998), as described by Laliberté et al. (2016); $K_d(\lambda)$ was computed using the SeaUV algorithm (Cao et al. 2014) from a monthly climatology of remote sensing reflectances (SeaWiFS sensor); $a_{CDOM}(\lambda)$ was computed with the model of Swan et al. (2013); μ_d was computed using the model of Kirk (1991). Note that, instead of a spectral μ_d, we used a broadband μ_d centered at 330 nm using as inputs the K_d and the total absorption and scattering coefficients at 330 nm estimated from pre-established bio-optical relationships. Additional analyses were performed to ensure consistency between the various optical sub-models (SM2). We assessed uncertainty by altering the input variables with Gaussian noise (SM3). Our calculations and the figures shown in the main article and SM can be reproduced with the code and datasets provided in a public repository (Galí et al. 2022), which requires Matlab® 2010b or later.

2.3 Pre-existing parameterizations

2.3.1 PAR-normalized photolysis rate constant

The spectrally-resolved model was compared with a simpler parameterization, named *K0_SCALED*, whereby $k_{p,z}$ is proportional to broadband visible irradiance:

$$k_{p,z} = k^{PAR}\, PAR_{0-} \cdot \exp(-K_d(490) \cdot z) \qquad \text{eq. 5}$$

where k^{PAR} is a rate constant normalized to broadband photosynthetically available radiation (PAR) that takes a fixed value with units of $[d^{-1}\ (\text{irradiance})^{-1}]$. Here we computed PAR_{0-} as the spectral integral of SBDART outputs between 400 and 700 nm, and vertical PAR attenuation using K_d at 490 nm from SeaUV.

This approach was employed in early DMS models (Vézina 2004) and later adopted in some global models (Bopp et al. 2008; Vogt et al. 2010) with varying k^{PAR} values. Here

we set $k^{PAR} = 0.0128$ m^2 (mol photons)$^{-1}$, the median of 111 globally distributed measurements of $k_{p,0-}$ divided by their corresponding SBDART-derived PAR_{0-} (Galí et al. 2016). This value facilitates comparisons between *K0_SCALED* and the spectral models derived from the same dataset (section 3.2). Alternative PAR-dependent formulations used in the PISCES model family, based on Belviso et al. (2012), are briefly discussed in 3.2 and analyzed in SM4.

2.3.2 Fixed photolysis rate constant

We tested an even simpler scheme, named *K0_FIXED*, that prescribes a fixed $k_{p,0-}$ regardless of subsurface irradiance, and attenuates $k_{p,z}$ following $K_d(490)$:

$$k_{p,z} = k^C_{p,0-} \exp(-K_d(490) \cdot z) \qquad \text{eq. 6}$$

Following Chu et al. (2003), here we set $k^C_{p,0-} = 0.5$ d^{-1}.

3. Results and Discussion

3.1 Spatiotemporal patterns

According to our model, DMS photolysis removes between 17.5 and 20.0 Tg S yr^{-1} from the upper mixed layer globally. The lower and upper bounds are obtained, respectively, when AQY(330) is estimated with the empirical parameterizations *CDOM_SST* (eq. 1B) or *CDOM_NO3* (eq. 1A). Sea-surface photolysis rate constants, $k_{p,0-}$, resulting from these AQY parameterizations agree within ±30% in 50% of the pixels on an annual basis, but differences are larger in the tropical Pacific and the Arctic (Fig. 3). Hence, although AQY is the main source of uncertainty in our estimates (SM3), the two equations likely provide realistic bounds for the estimation of global DMS photolysis.

Taking the *CDOM_NO3* model as a reference, we obtain a global area-weighted mean $k_{p,0-}$ of 0.44 d^{-1} (all means reported hereafter are weighted by pixel area). Although the mean $k_{p,0-}$ is higher during the summer, as expected from the seasonal cycle of irradiance, relatively large spatial variations are observed, reflecting spatial AQY variability (Fig. 2). Mixed-layer mean rate constants, $k_{p,ML}$, show wider seasonality than $k_{p,0-}$ (Fig. 2). This

pattern arises from the shoaling of the UML during the summer, itself a result of high solar irradiance, which implies that a larger fraction of the UML experiences high UV exposure, hence bringing $k_{p,ML}$ closer to $k_{p,0-}$.

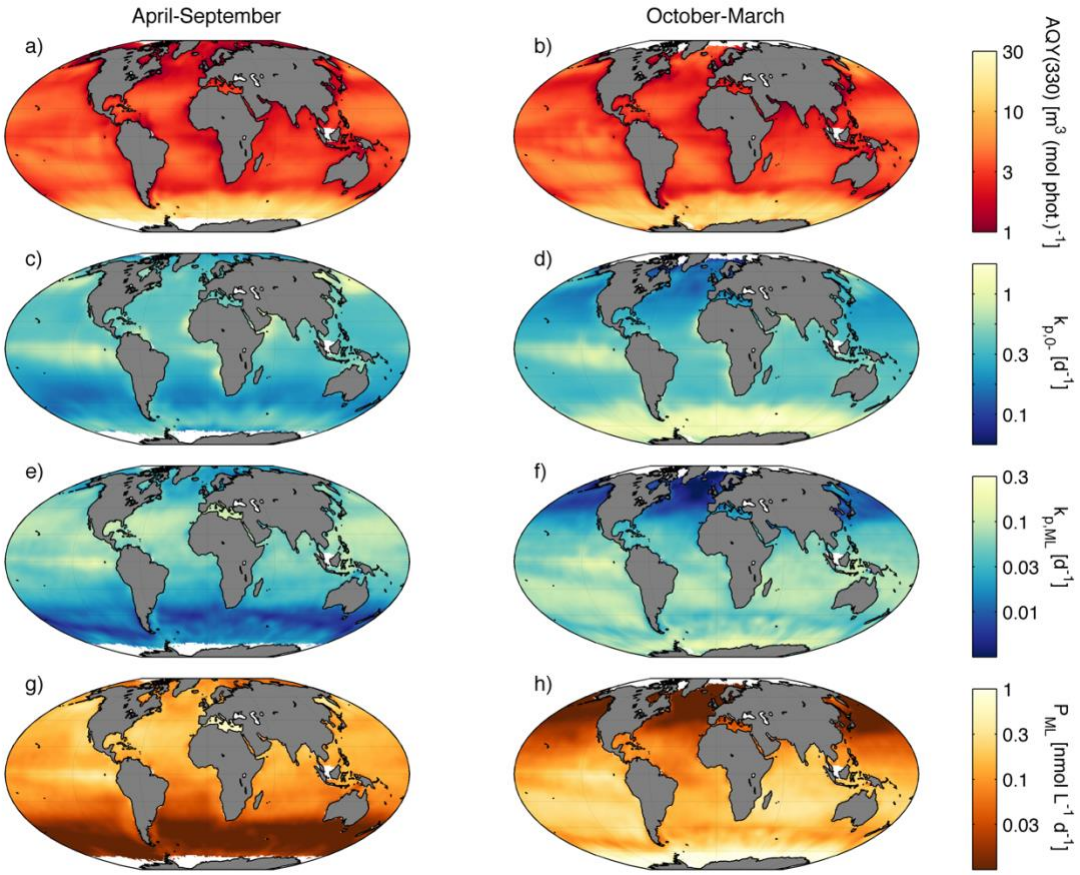

Figure 2. *Global DMS photolysis rates estimated with an empirical model and satellite data: (a, b) DMS photolysis apparent quantum yield at the reference wavelength, AQY(330); (c, d) daily mean photolysis rate constants at the sea surface (k_{p0-}); (e, f) daily mean photolysis rate constants in the upper mixed layer ($K_{p,ML}$); (g, h) photolysis rates in the upper mixed layer. Left and right panels show, respectively, the means for the boreal (a, c, d, g) and austral (b, d, f, h) summer semesters centered on the solstices.*

Photolysis rates are calculated from the product of $k_{p,ML}$ and a monthly climatology of sea-surface DMS concentration. Since DMS concentrations peak during the summer and are generally higher in subpolar and polar latitudes, summertime photolysis rates are further intensified at high latitudes in comparison to $k_{p,ML}$. These general patterns hold

when the default DMS fields, provided by the most recent climatology (Hulswar et al. 2022), are replaced by the previous climatology (Lana et al. 2011). The older climatology produces slightly lower global DMS photolysis rates (16.8–19.8 Tg S yr^{-1}), despite having 4% higher DMS concentration globally, because of differences in the spatiotemporal DMS distribution.

Meridional asymmetry is possibly the most conspicuous feature in global DMS photolysis rates. Around 73% of the total annual photolysis occurs in the Southern Hemisphere, which accounts for 57% of the ocean area, and ~35% occurs south of 40°S, within 21% of the ocean area. This feature has not been reported for other photochemical processes, and results primarily from the high AQYs observed in the Southern Ocean (Toole et al. 2004), which are one order of magnitude higher than elsewhere (Fig. 2). High AQYs counteract the prevailing low irradiance in the Southern Ocean (Fig. S2), such that $k_{p,0-}$ south of 40°S are 62% higher than the global average (Fig. 2). Deep mixing plays a dual role in the Southern Ocean: it lowers $k_{p,ML}$ to 0.040 d^{-1}, slightly below the global mean of 0.052 d^{-1}, but increases total photolysis because the rates are integrated over a thicker layer.

In our spectral model, vertical attenuation of $k_{p,z}$ is variable by construction. To depict this variability, we computed the linear regression between $\ln(k_{p,z})$ and depth for each pixel and month. The resulting regression slope is $K_d(k_{p,z})$, the $k_{p,z}$ vertical attenuation coefficient. Over the first two optical depths, $K_d(k_{p,z})$ is generally within 10% of $K_d(330)$ (Fig. S2), and typically ranges between 0.09–0.28 m^{-1} (68% central values). On a global average, the 10% attenuation depth of $k_{p,z}$ is 14.5 m. Thus, DMS photolysis is usually confined in the UML. If we assume that sea-surface a_{CDOM} and AQY can be extrapolated below the UML, and do not truncate photolysis at z=MLD, the integral of $k_{p,z}$ increases by only 9% globally. This result agrees with global models of photochemical processes that show similar spectral dependence (Fichot and Miller 2010; Zhu and Kieber 2020).

3.2 Simplified parameterizations: caveats and potential improvement

Global DMS photolysis estimates based on the schemes *K0_FIXED* and *K0_SCALED*,

representative of current biogeochemical models, exceed our best estimates by more than twofold (Table 1). The main reason for this overestimation is that they attenuate photolysis vertically following PAR rather than UV radiation. Indeed, PAR-dependent $k_{p,z}$ penetrates much deeper in the water column, with an average 10% attenuation depth of 56 m. Consequently, these schemes overestimate photolysis in the UML (Fig. 3), but also below it. Also note that, unlike the simplified schemes, our spectral photolysis model is proportional to scalar downwelling irradiance, the quotient between planar irradiance and the mean cosine (E_d/μ_d). Accounting for μ_d (i.e., the tridimensional light field) in the simplified models would exacerbate their positive bias.

Table 1. *DMS photolysis rates (Tg S per period) obtained with our spectral model using two alternative parameterizations (CDOM_NO3 and CDOM_SST) and with two simplified parameterizations used in global biogeochemical models.*

Model	*Northern Hemisphere*			*Southern Hemisphere*			*Global*
	Apr-Sep	Oct-Mar	**Year**	Apr-Sep	Oct-Mar	**Year**	**Year**
CDOM_NO3 [a]	3.6	1.8	**5.4**	2.8	11.7	**14.5**	**20.0**
CDOM_SST [b]	3.0	1.3	**4.3**	2.2	10.9	**13.1**	**17.5**
K0_SCALED [c]	10.2	5.9	**16.1**	9.1	20.0	**29.1**	**45.2**
K0_FIXED [d]	9.2	6.9	**16.1**	11.8	19.5	**31.2**	**47.3**

[a] eq. 1A: Fit between AQY330 and $a_{CDOM,330}$ and NO_3^-.

[b] eq. 1B: Fit between AQY330 and $a_{CDOM,330}$ and SST with an interaction term.

[c] eq. 5: $k_{p,z}$ scaled to PAR_z as in Vogt et al. 2010, with modified parameters.

[d] eq. 6: fixed $k_{p,0-}$ as in Chu et al. 2003.

The global average $k_{p,0-}$ simulated with the simplified schemes (0.45–0.50 d^{-1}) and with the *CDOM_NO3* scheme (0.44 d^{-1}) are in good agreement. Yet, they show distinct spatial deviations (Fig. 3). Surprisingly, *K0_FIXED* shows better agreement with the reference fields than *K0_SCALED* in terms of their annual mean $k_{p,0-}$. Indeed, prescribing a fixed $k_{p,0-}$ is unrealistic in extratropical regions with a marked seasonal cycle of irradiance. The *K0_SCALED* scheme exhibits a positive (negative) deviation at low (high) latitudes, with particularly negative bias in the Southern Ocean. In the Belviso et al. (2012) and subsequent PISCES model versions this spatial bias is corrected by adding a nitrate-

dependent photolysis term. However, these newer versions adopted a Michaelis-Menten formulation for both PAR- and nitrate-dependent photolysis, which is not supported by measurements (Kieber et al. 1996; Bouillon and Miller 2004; Toole et al. 2004).

In section SM4 and Table S2 we review the value of k^{PAR} in different models, which determine each model's biases together with PAR forcing fields. Significantly, we found an order-of-magnitude error in the value of the k^{PAR} parameter that apparently creeped from the text of Lefèvre et al. (2002) and Vézina (2004) into, at least, the codes of Bopp et al. (2008) and Vogt et al. (2010). We therefore recommend that future model studies provide more careful descriptions of their parameters and forcing fields.

As a corollary to this subsection, we compare eq. 4–6 to analyze the implicit assumptions made in each simplified scheme and evaluate their validity. Whereas *K0_FIXED* assumes that the spectral integral $\int E_{d,0^-}(\lambda)\cdot a_{CDOM}(\lambda)\cdot AQY(\lambda)\, d\lambda$ is constant, the *K0_SCALED* scheme assumes that only $\int a_{CDOM}(\lambda)\cdot AQY(\lambda)\, d\lambda$ is constant. For different reasons, none of these assumptions holds when evaluated against our spectral model forced by seasonally varying irradiance. By construction, the *K0_SCALED* scheme allows for more realistic seasonality and could be readily improved by (i) prescribing spatial k^{PAR} arrays adjusted to match the spectral model outputs, and (ii) empirically correcting the vertical attenuation of $k_{p,z}$, $K_d(k_{p,z})$ (see 3.1). The latter can be estimated from remotely sensed $K_d(490)$ using this regression equation: $K_d(k_{p,z}) = 1.9854\cdot[K_d(490)^{1.0713}]$, with $R^2 = 0.83$. This fit provides a direct means to correct $K_d(490)$ in eq. 5.

3.3 Limitations of the spectral model

With a mean absolute error of around 70% (Fig. 1 and S1), the AQY(λ) parameterizations are the largest source of uncertainty in our approach (SM3, Fig. S3 and Table S1). It is worth noting that, with the aim of maximizing the explained AQY(330) variance, nitrate and SST are used as empirical predictors (eq. 1). Thus, their coefficients do not reflect their mechanistic effects on AQY(330), or account for additional causes of spatial AQY(330) variation that remain poorly understood. Galí et al. (2016) found a consistent nitrate-dependent increase of AQY(330) through meta-analysis of data from different

locations (Bouillon and Miller 2004; Toole et al. 2004). Yet, this effect could not explain the AQY(330) variability left after removing the a_{CDOM}-dependent variability. The same study found that temperature effects on photolysis kinetics were not consistent across locations. New in-situ studies are needed to develop more mechanistic (and eventually more precise) representations of AQY variability. Such studies should consider CDOM composition, the presence of other photosensitizers, temperature effects, and their impact on AQY seasonality, which could not be validated in our model. Additional uncertainties arising from satellite retrievals and optical modelling are discussed in SM1–3.

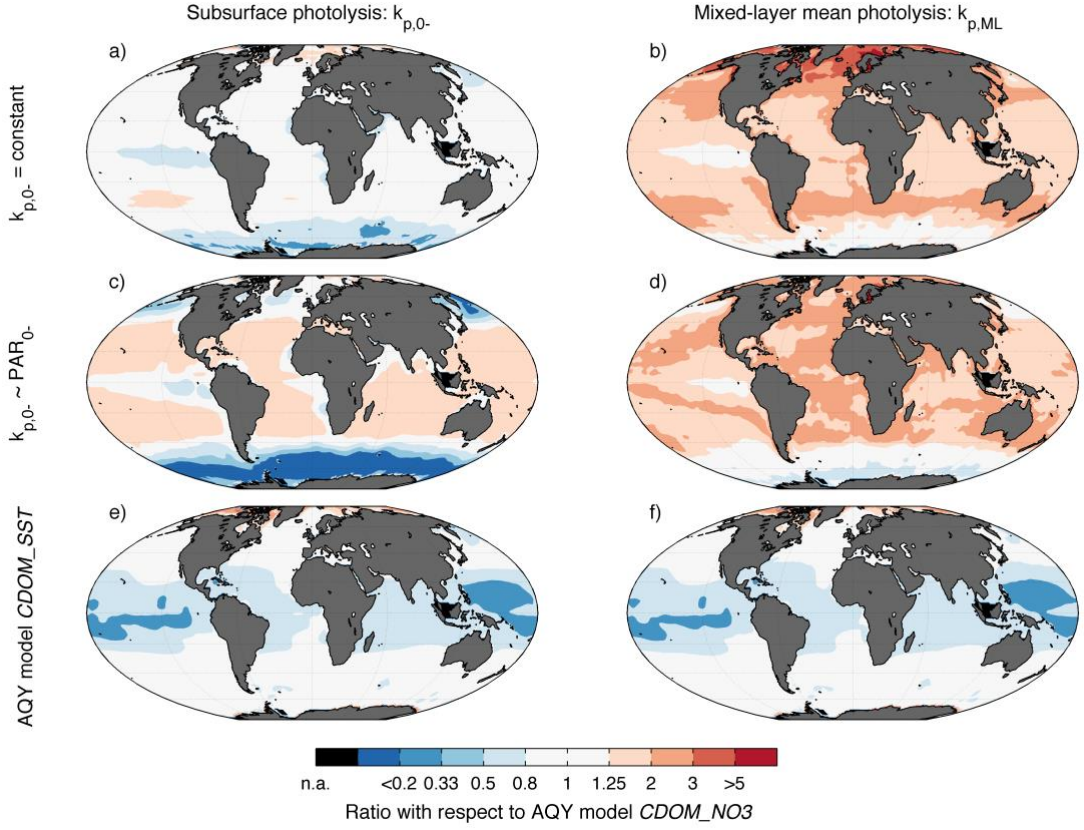

Figure 3*. Comparison between annual mean photolysis rate constants for DMS at the sea surface (left) and the upper mixed layer (right) obtained with different parameterizations (rows), expressed as their ratio with respect to the reference model (spectral model with AQY as a function of CDOM and NO_3^-): (a, b) K0_FIXED model with constant sub-surface photolysis rate constant $k_{p,0-}$; (c, d) K0_SCALED model with $k_{p,0-}$ proportional to subsurface PAR_{0-}; (e, f) spectral model with AQY as a function of CDOM and SST.*

3.4 Concluding remarks

Calculations based on the meta-analysis of in situ data suggested that photolysis was a larger sink for DMS in the UML than emission to the atmosphere (Galí and Simó 2015). However, our results imply that this is not the case but rather that photolysis removes approximately 30% less DMS than the 27 Tg S yr^{-1} removed by sea-air gas exchange (Hulswar et al. 2022). The bias of in situ sampling towards the summer season likely explains this discrepancy (Galí and Simó 2015). This unexpected conclusion of our study demonstrates the importance of using Earth observation data to extrapolate in situ rates to large scales.

Surface Southern Ocean waters stand out as a DMS photolysis hotspot globally. Secondary aerosols derived from atmospheric DMS oxidation play a key role in this region because of the low influence of anthropogenic and terrestrial aerosol sources and the summer minimum in primary marine aerosol (Fiddes et al. 2018; Fossum et al. 2018). Further work is warranted to understand the relative impact of photolysis and other DMS sinks in controlling DMS emission in this climatically important area.

Acknowledgments

We thank the NASA Ocean Biology Distributed Active Archive Center (OB.DAAC) for access to satellite data, Maxime Benoît-Gagné for guidance with radiative transfer computations and the Takuvik Joint International Laboratory (CNRS-France and Univeristé Laval-Canada) for access to computing facilities. MG received funding from a Beatriu de Pinós postdoctoral fellowship (AGAUR, Generalitat de Catalunya).

References

Belviso, S., I. Masotti, A. Tagliabue, and others. 2012. DMS dynamics in the most oligotrophic subtropical zones of the global ocean. Biogeochemistry **110**: 215–241. doi:10.1007/s10533-011-9648-1

Bock, J., M. Michou, P. Nabat, and others. 2021. Evaluation of ocean dimethylsulfide concentration and emission in CMIP6 models. Biogeosciences **18**: 3823–3860. doi:10.5194/bg-18-3823-2021

Bopp, L., O. Aumont, S. Belviso, and S. Blain. 2008. Modelling the effect of iron fertilization on dimethylsulphide emissions in the Southern Ocean. Deep Sea Res. Part II **55**: 901–912. doi:10.1016/j.dsr2.2007.12.002

Bouillon, R.-C., and W. L. Miller. 2004. Determination of apparent quantum yield spectra of DMS photo-degradation in an in situ iron-induced Northeast Pacific Ocean bloom. Geophys. Res. Lett. **31**: L06310. doi:10.1029/2004GL019536

Brimblecombe, P., and D. Shooter. 1986. Photo-oxidation of dimethylsulphide in aqueous solution. Mar. Chem. **19**: 343–353.

Cao, F., C. G. Fichot, S. B. Hooker, and W. L. Miller. 2014. Improved algorithms for accurate retrieval of UV/visible diffuse attenuation coefficients in optically complex, inshore waters. Remote Sens. Environ. **144**: 11–27. doi:10.1016/j.rse.2014.01.003

Carslaw, K. S., L. a Lee, C. L. Reddington, and others. 2013. Large contribution of natural aerosols to uncertainty in indirect forcing. Nature **503**: 67–71. doi:10.1038/nature12674

Charlson, R. J., J. E. Lovelock, M. O. Andreae, and S. G. Warren. 1987. Oceanic phytoplankton, atmospheric sulphur, cloud albedo and climate. Nature **326**: 655–661. doi:10.1038/326655a0

Chu, S., S. Elliott, and M. E. Maltrud. 2003. Global eddy permitting simulations of surface ocean nitrogen, iron, sulfur cycling. Chemosphere **50**: 223–235. doi:10.1016/S0045-6535(02)00162-5

Le Clainche, Y., A. Vézina, M. Levasseur, and others. 2010. A first appraisal of prognostic ocean DMS models and prospects for their use in climate models. Global Biogeochem. Cycles **24**: GB3021. doi:10.1029/2009GB003721

Fichot, C. G., and W. L. Miller. 2010. An approach to quantify depth-resolved marine photochemical fluxes using remote sensing: Application to carbon monoxide (CO) photoproduction. Remote Sens. Environ. **114**: 1363–1377. doi:10.1016/j.rse.2010.01.019

Fiddes, S. L., M. T. Woodhouse, Z. Nicholls, T. P. Lane, and R. Schofield. 2018. Cloud, precipitation and radiation responses to large perturbations in global dimethyl sulfide. Atmos. Chem. Phys. **18**: 10177–10198.

Fossum, K. N., J. Ovadnevaite, D. Ceburnis, and others. 2018. Summertime Primary and

412 Secondary Contributions to Southern Ocean Cloud Condensation Nuclei. Sci. Rep.
413 **8**: 1–14. doi:10.1038/s41598-018-32047-4
414 Galí, M., D. J. Kieber, C. Romera-Castillo, and others. 2016. CDOM Sources and
415 Photobleaching Control Quantum Yields for Oceanic DMS Photolysis. Environ. Sci.
416 Technol. **50**: 13361–13370. doi:10.1021/acs.est.6b04278
417 Galí, M., G. L. Pérez, and E. C. Devred. 2022. Global ocean dimethylsulfide (DMS)
418 photolysis model.doi:10.5281/zenodo.7204133
419 Galí, M., and R. Simó. 2015. A meta-analysis of oceanic DMS and DMSP cycling
420 processes: Disentangling the summer paradox. Global Biogeochem. Cycles **29**: 496–
421 515. doi:10.1002/2014GB004940
422 Hulswar, S., R. Simó, M. Galí, and others. 2022. Third revision of the global surface
423 seawater dimethyl sulfide climatology (DMS-Rev3). Earth Syst. Sci. Data **14**: 2963–
424 2987. doi:10.17632/hyn62spny2.1
425 Kieber, D. J., J. Jiao, R. P. Kiene, and T. S. Bates. 1996. Impact of dimethylsulfide
426 photochemistry on methyl sulfur cycling in the equatorial Pacific Ocean. J.
427 Geophys. Res. **101**: 3715–3722. doi:10.1029/95JC03624
428 Kirk, J. T. O. 1991. Volume scattering function, average cosines, and the underwater
429 light field. Limnol. Oceanogr. **36**: 455–467. doi:10.4319/lo.1991.36.3.0455
430 Laliberté, J., S. Bélanger, and R. Frouin. 2016. Evaluation of satellite-based algorithms to
431 estimate photosynthetically available radiation (PAR) reaching the ocean surface at
432 high northern latitudes. Remote Sens. Environ. **184**: 199–211.
433 doi:10.1016/j.rse.2016.06.014
434 Lana, A., T. G. Bell, R. Simó, and others. 2011. An updated climatology of surface
435 dimethlysulfide concentrations and emission fluxes in the global ocean. Global
436 Biogeochem. Cycles **25**: GB1004. doi:10.1029/2010GB003850
437 Lefèvre, M., A. Vézina, M. Levasseur, and J. W. H. Dacey. 2002. A model of
438 dimethylsulfide dynamics for the subtropical North Atlantic. Deep. Res. Part I
439 Oceanogr. Res. Pap. **49**: 2221–2239. doi:10.1016/S0967-0637(02)00121-8
440 Ricchiazzi, P., S. Yang, C. Gautier, and D. Sowle. 1998. SBDART: A Research and
441 Teaching Software Tool for Plane-Parallel Radiative Transfer in the Earth's
442 Atmosphere. Bull. Am. Meteorol. Soc. **79**: 2101–2114. doi:10.1175/1520-

0477(1998)079<2101:SARATS>2.0.CO;2

Schmidtko, S., G. C. Johnson, and J. M. Lyman. 2013. MIMOC: A global monthly isopycnal upper-ocean climatology with mixed layers. J. Geophys. Res. Ocean. **118**: 1658–1672. doi:10.1002/jgrc.20122

Shaw, G. E. 1983. Bio-controlled thermostasis involving the sulfur cycle. Clim. Change **5**: 297–303. doi:10.1007/BF02423524

Swan, C. M., N. B. Nelson, D. A. Siegel, and E. A. Fields. 2013. A model for remote estimation of ultraviolet absorption by chromophoric dissolved organic matter based on the global distribution of spectral slope. Remote Sens. Environ. **136**: 277–285. doi:10.1016/j.rse.2013.05.009

Tesdal, J.-E., J. R. Christian, A. H. Monahan, and K. von Salzen. 2016. Evaluation of diverse approaches for estimating sea-surface DMS concentration and air-sea exchange at global scale. Environ. Chem. **13**: 390–412. doi:10.1071/EN14255

Toole, D. A., D. J. Kieber, R. P. Kiene, D. A. Siegel, and N. B. Nelson. 2003. Photolysis and the dimethylsulfide (DMS) summer paradox in the Sargasso Sea. Limnol. Oceanogr. **48**: 1088–1100. doi:10.4319/lo.2003.48.3.1088

Toole, D. A., D. J. Kieber, R. P. Kiene, E. M. White, J. Bisgrove, D. A. del Valle, and D. Slezak. 2004. High dimethylsulfide photolysis rates in nitrate-rich Antarctic waters. Geophys. Res. Lett. **31**: L11307. doi:10.1029/2004GL019863

del Valle, D., D. J. Kieber, and R. P. Kiene. 2007. Depth-dependent fate of biologically-consumed dimethylsulfide in the Sargasso Sea. Mar. Chem. **103**: 197–208. doi:10.1016/j.marchem.2006.07.005

del Valle, D., D. J. Kieber, D. A. Toole, J. Brinkley, and R. P. Kiene. 2009. Biological consumption of dimethylsulfide (DMS) and its importance in DMS dynamics in the Ross Sea, Antarctica. Limnol. Oceanogr. **54**: 785–798.

Vézina, A. F. 2004. Ecosystem modelling of the cycling of marine dimethylsulfide: A review of current approaches and of the potential for extrapolation to global scales. Can. J. Fish. Aquat. Sci. **61**: 845–856. doi:10.1139/F04-025

Vogt, M., S. M. Vallina, E. T. Buitenhuis, L. Bopp, and C. Le Quéré. 2010. Simulating dimethylsulphide seasonality with the Dynamic Green Ocean Model PlankTOM5. J. Geophys. Res. **115**: 1–21. doi:10.1029/2009JC005529

Zhu, Y., and D. J. Kieber. 2020. Global Model for Depth-Dependent Carbonyl Photochemical Production Rates in Seawater. Global Biogeochem. Cycles **34**: e2019GB006431. doi:10.1029/2019GB006431

Supplemental Materials

For the article

Global ocean dimethylsulfide photolysis rates quantified with a spectrally and vertically resolved model

Martí Galí[1]*, Emmanuel Devred[2], Gonzalo L. Pérez[3], David J. Kieber[4], Rafel Simó[1]

[1]Institut de Ciències del Mar, CSIC, Passeig Marítim de la Barceloneta 37-49, 08003 Barcelona, Catalonia, Spain

[2]Fisheries and Oceans Canada, Bedford Institute of Oceanography, Dartmouth, NS B2Y 4A2, Canada

[3]Instituto INIBIOMA (CRUB Comahue, CONICET), Quintral 1250, 8400 S.C. de Bariloche, Rio Negro, Argentina

[4] Department of Chemistry, State University of New York, College of Environmental Science and Forestry, 1 Forestry Drive, Syracuse, New York 13210, United States

* Corresponding author: mgali@icm.csic.es

Keywords: DMS; UV radiation; photolysis; remote sensing; photochemical model; CDOM; photosensitizer; ocean.

Data availability statement: Data and code are available in https://doi.org/10.5281/zenodo.7204133.

Content: In SM1 and SM2 we describe the sub-models used to estimate the different components of the DMS photolysis equation (eq. 4 of the main text). In SM3 we report uncertainty assessment results. In SM4 we compare the parameterizations used in the DMS modules of several global biogeochemistry models.

SM1. Monthly climatology of sea-surface spectral irradiance

Downwelling spectral irradiance was computed using the Santa Barbara DISORT Atmospheric Radiative Transfer (SBDART) model (Ricchiazzi et al. 1998), a plane-parallel atmospheric radiative transfer model. Our specific SBDART implementation has been described and validated in previous works (Laliberté et al. 2016; Ayyala Somayajula et al. 2018). In this configuration, SBDART outputs the spectral irradiance (μmol quanta m^{-2} s^{-1} nm^{-1}) at a given location and time at a spectral resolution of 5 nm between 290 and 700 nm.

First, we calculated a five-dimensional look-up table (LUT) for spectral irradiance just below the water surface, $E_{d,0-}(\lambda)$ as a function of (i) wavelength (λ): 290 to 700 nm at 5-nm intervals; (ii) solar zenith angle (SZA): 0 to 90 degrees at 5° intervals; (iii) total ozone column: 100 to 550 Dobson units (DU) at 50-DU intervals; (iv) cloud optical thickness (COT): 0 to 64 in powers of 2 intervals (2^n, n from 0 to 6); and (v) surface albedo (A): 0.05 to 0.95 in 0.15 intervals. We additionally prescribed a constant aerosol optical depth of 0.05 at 550 nm representative of marine aerosols and vertical profiles of pressure, temperature, and water vapor profiles for a standard marine summer atmosphere. Total $E_{d,0-}(\lambda)$ was calculated as the sum of diffuse and direct irradiance considering their different reflection at the sea surface, following Fresnel's law for the direct component and assuming 6.6% reflectance for the diffuse component.

Second, for a given location and time, the LUT was interpolated using the input values provided by satellite observations. In this step, $E_{d,0-}(\lambda)$ was calculated under two situations: for a cloud-free sky, $E_{d,0-,CLEAR}(\lambda)$ (COT = 0), and for the satellite observed COT, $E_{d,0-,CLOUD}(\lambda)$. The final output was calculated as the mean of cloudy and cloud-free irradiance, weighted by the mean daily cloud fraction (CF):

$$E_{d,0-}(\lambda) = E_{d,0-,CLOUD}(\lambda) \times CF + E_{d,0-,CLEAR}(\lambda) \times (1 - CF) \quad \text{(eq. S1)}$$

Satellite observations of the total ozone column, COT and CF were obtained from the Level-3 MODIS-Aqua atmosphere gridded product at daily 1°x1° resolution (Collection 005, MYD08_D3, https://modis-images.gsfc.nasa.gov/products_C005update.html).

Third, we used this setup to create a global monthly climatology at 5°x5° resolution by querying satellite data at the center of each 5°x5° macropixel. For a given day, spectral irradiance was calculated over 3 h intervals centered at 01:30, 04:30… and 22:30 (UTC time) to account for variations in SZA, obtaining an array with 83 wavelengths and 8 times. We computed $E_{d,0-}(\lambda)$ for the days 5, 15 and 25 of each month, and averaged the three arrays to obtain a monthly mean 83×8 array.

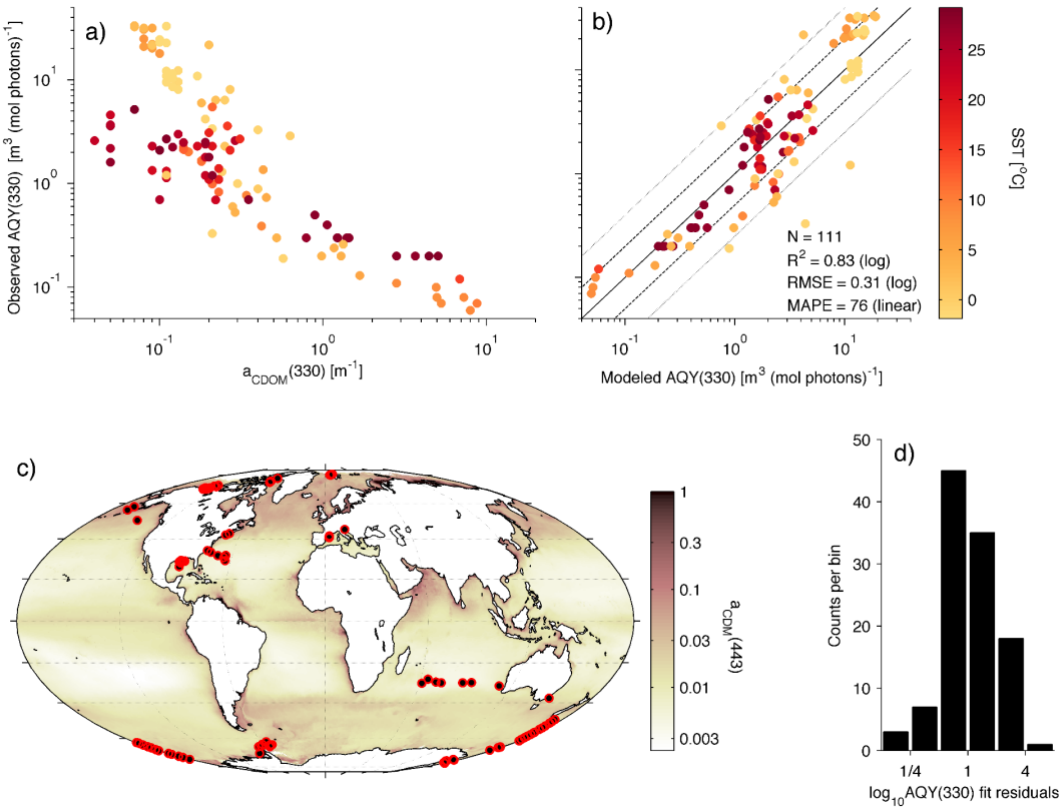

Figure S1. *As Fig. 1 of the main text but with $a_{CDOM}(330)$ and SST as predictors (eq. 1B).*

SM2. Underwater optics and irradiance fields

CDOM absorption spectra were estimated with a method (Swan et al. 2013) that exploits the nonlinear relationships between CDOM absorption coefficients, their spectral slopes between 320 and 400 nm, and the absorption coefficient of chromophoric detrital matter at 443 nm, $a_g(443)$. The latter is retrieved with the Garver-Siegel-Maritorena (GSM) semi-analytical algorithm (Maritorena et al. 2002). We applied Swan et al. (2013) algorithm to the full spectral range 290 and 500 nm, although the algorithm was not validated in the 325–412 nm spectral range. Given the typical exponential shape of CDOM spectra, we do not expect significant deviations in the vicinity of these validation wavelengths. Our calculations indicate that more than two thirds of total photolysis occur between 325 and 412 nm, such that algorithm inaccuracies outside this spectral region have a limited impact on total photolysis rate

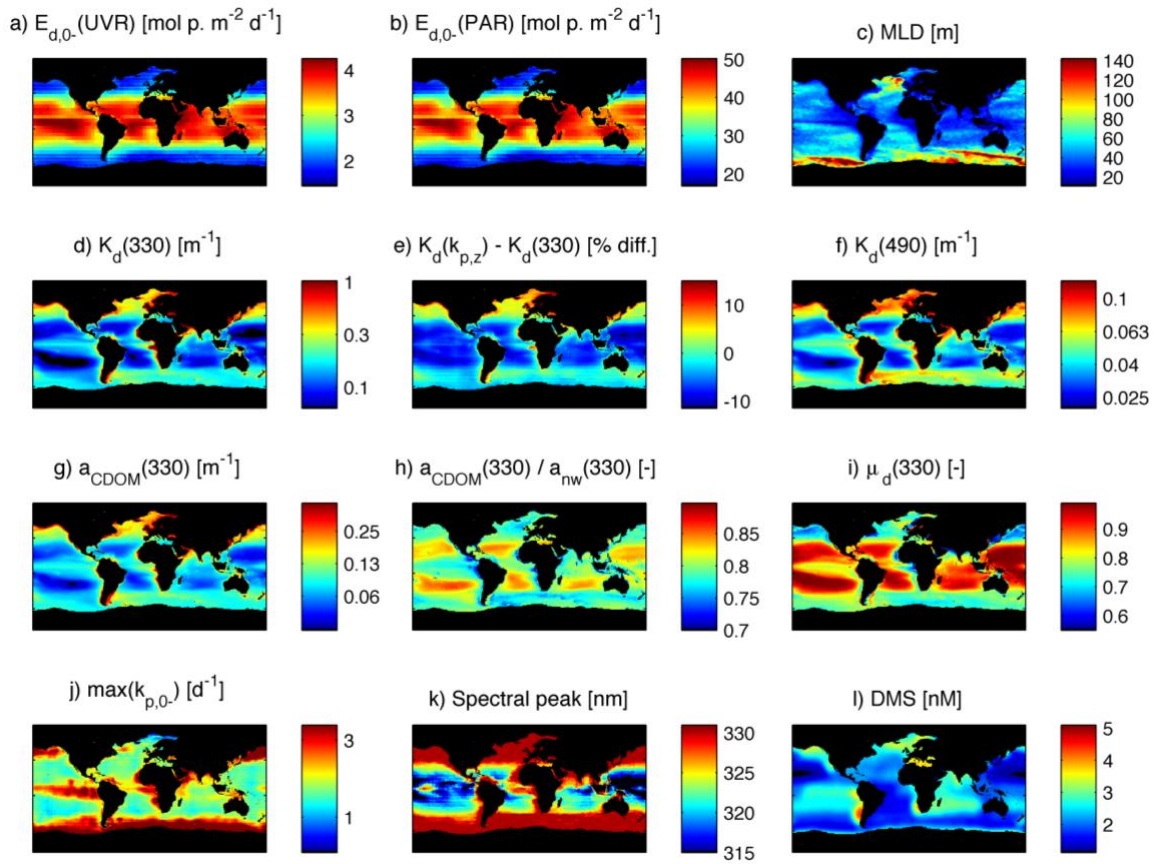

559

560 ***Figure S2****. Summary of the global annual mean distributions of relevant variables*
561 *involved in, or resulting from, the calculation of spectrally resolved DMS photolysis.*

562 The spectral irradiance just below the sea surface was propagated downwards using the
563 $K_d(\lambda)$ estimated with the SeaUV algorithm (Cao et al. 2014), using as input a climatology
564 of remote sensing reflectances from the SeaWiFS sensor (412, 443, 490, 510, 555 and
565 670 nm). The SeaUV outputs (K_d at 320, 340, 380, 412, 443 and 490 nm) were spectrally
566 interpolated to 5 nm resolution using the Matlab function 'interp1' with piecewise cubic
567 Hermite interpolation ('pchip'). The same method was used to extrapolate their values
568 between 320 nm and 290 nm.

569 The mean cosine of downwelling irradiance at 330 nm, $\mu_d(330)$, was estimated by
570 inverting the model of Kirk (1991), by which:

571 $$K_d(\lambda) = \mathrm{srqt}\{ [a(\lambda)]^2 + G1 \cdot a(\lambda) \cdot b(\lambda) \} / \mu_d(\lambda) \quad \text{(eq. S2)}$$

572 We set the dimensionless coefficient G1 = 0.126 (Pérez et al. 2016), and computed the
573 total absorption and scattering coefficients at 330 nm as follows:

574 $$a(330) = a_w(330) + a_{phy}(330) + a_{nap}(330) + a_{CDOM}(330) \quad \text{(eq. S3)}$$

$$b(330) = b_w(330) + b_p(330) \quad \text{(eq. S4)}$$

For pure seawater absorption and scattering coefficients we used the values tabulated in Morel et al. (2007), $a_w(330) = 0.009\ m^{-1}$ and $b_w(330) = 0.0152\ m^{-1}$. To estimate the particulate absorption coefficient at 330 nm we used pre-computed bio-optical relationships making some simplifying assumptions. First, we estimated phytoplankton light absorption at 440 nm using eq. 2 of Bricaud et al. (1998),

$$a_{phy}(440) = 0.0378\ Chl^{0.627} \quad \text{(eq. S5)}$$

where Chl is the chlorophyll *a* concentration at the sea surface; second, we assumed that $a_{phy}(330) = a_{phy}(440)$ following the results shown in Fig. 5 of Bricaud et al. (2010), which covered waters with wide-ranging trophic status. Although rough, this assumption provides a plausible central value for the relationship between $a_{phy}(330)$ and $a_{phy}(440)$ in the absence of a simple model of general applicability for $a_{phy}(330)$. Other studies found similar results in meso- to oligotrophic Mediterranean waters (e.g. Pérez et al., 2021); third, we estimated non-algal particulate absorption using eq. 3 of Bricaud et al. (1998),

$$a_{nap}(440) = 0.0124\ Chl^{0.724} \quad \text{(eq. S6)}$$

and used the spectral slope of $0.010\ nm^{-1}$ provided by Bricaud et al. (2010) (text and their Fig. 12) to estimate a_{nap} at 330 nm,

$$a_{nap}(330) = a_{nap}(440)\cdot\exp[-0.010\cdot(330-440)] \quad \text{(eq. S7)}$$

To calculate the particulate scattering coefficient at 330 nm we started from the equation given in Table 2 of Loisel and Morel (1998), which estimates the beam attenuation coefficient at 660 nm from Chl concentration:

$$c_p(660) = 0.347\ Chl^{0.766} \quad \text{(eq. S8)}$$

We then followed Organelli et al. (2020) (eq. 2, Fig. 8 and text) to estimate the beam attenuation coefficient at 330 nm:

$$c_p(330) = c_p(660)\ [(330/660)^{-0.95}] \quad \text{(eq. S9)}$$

Finally, the particulate scattering coefficient at 330 nm was calculated by subtracting particulate absorption from total beam attenuation,

$$b_p(330) = c_p(330) - a_p(330) \quad \text{(eq. S10)}$$

This approach has the advantage of the reciprocal compensation of biases between $b_p(330)$ and $a_p(330)$, whose total value remains bounded by $c_p(330)$.

Finally, scalar downwelling spectral irradiance was computed as $E_d(\lambda)/\mu_d(330)$, assuming that $\mu_d(330)$ can be applied to other wavelengths because the photolysis spectrum is

heavily weighted towards wavelengths around 330 nm. Following previous studies (Fichot and Miller 2010; Zhu and Kieber 2020) we neglected upwelling irradiance because, at UV wavelengths that drive DMS photolysis, absorption coefficients are generally much larger than scattering coefficients and therefore dominate light attenuation. Under such conditions, the underwater light field is very directional (as opposed to diffuse) and the cosine of underwater downwelling irradiance approaches 1. As can be seen in Fg. S2, $\mu_d(330)$ is typically >0.9 in oligotrophic gyres and <0.8 in temperate and (sub)polar regions. This results from the relatively larger particle load in more productive waters, which lowers the contribution of CDOM to total non-water absorption (a_{nw}) and simultaneously increases particulate scattering. Hence, neglecting upwelling irradiance may cause a larger negative bias to DMS photolysis in temperate and (sub)polar waters than in oligotrophic waters.

In summary, despite the uncertainties involved in the calculation of $\mu_d(330)$ through several intermediate steps, its geographical patterns appear consistent with those of better-known bio-optical quantities like Chl and a_{CDOM}. The global mean value of $\mu_d(330)$ is 0.82. Its inverse, 1.22, is the mean correction factor applied to E_d and is very close to the constant factor of 1.2 previously used to model DMS photolysis in the Sargasso Sea (Toole et al. 2003). Sargasso Sea waters oscillate between ultraoligotrophic conditions in late summer and mesotrophic conditions during late winter. Based on radiative transfer calculations for clear and cloudy skies and solar elevations typical of summer and winter, the latter study reported a total range for this correction factor between 1.15 and 1.29, which corresponds to μ_d between 0.78 and 0.87. For comparison, the annual range in $\mu_d(330)$ produced by our approach at the same location (31°40′N 64°10′W) is 0.77–0.94.

Satellite datasets for $a_g(443)$, Chl, remote sensing reflectance spectra and $K_d(490)$ were downloaded from the NASA Ocean Color website (https://oceancolor.gsfc.nasa.gov/; last accessed on 12 May 2015). The global monthly climatologies from the SeaWiFS sensor (1997–2010 period) were re-gridded from 1/12° to 1° resolution.

SM3. Uncertainty assessment

Following previous studies (Fichot and Miller 2010; Zhu and Kieber 2020), sensitivity analyses were conducted by computing global monthly $k_{p,ML}$ fields with altered inputs of AQY(λ), $a_{CDOM}(\lambda)$, $K_d(\lambda)$, $E_{d,0^-}(\lambda)$ and Chl (which is used to compute μ_d, section SM2). The input variables were altered by adding Gaussian noise according to the equation:

$$V_{altered}(\lambda) = V(\lambda) + V(\lambda)\cdot\varepsilon(\lambda)\cdot\gamma \qquad \text{(eq. S11)}$$

where $V_{altered}(\lambda)$ and $V(\lambda)$ represent the altered and the original input variables, and γ is the set percentage error, here defined as the mean absolute percentage error (MAPE; often referred to as mean absolute percentage deviation).

We used $\gamma = 70\%$ for AQY(λ), $\gamma = 30\%$ for bio-optical variables ($K_d(\lambda)$, $a_{CDOM}(\lambda)$ and Chl) and $\gamma = 10\%$ for $E_{d,0^-}(\lambda)$. These values are deemed representative of each variable's uncertainty (see below).

In the case of Chl, the perturbation was applied as a normally distributed ε with mean = 0 and standard deviation = $1/\sqrt{2\pi}$. The latter expression is needed to translate the set percentage error γ, i.e., MAPE, into standard deviation.

In the case of spectral variables, the random noise was expressed as:

$$\varepsilon(\lambda) = U \cdot \varepsilon_U(\lambda) \cdot + C \cdot \varepsilon_C(\lambda) \qquad \text{(eq. S12)}$$

where ε_U represents spectrally uncorrelated noise (a different error at every wavelength) and ε_C represents a constant error for the whole spectrum. Both errors are generated randomly based on a normal distribution with mean = 0 and standard deviation = $1/\sqrt{2\pi}$. U and C are the fractions of ε_U and ε_C , and U + C = 1. According to the results of the previous studies where different U and C values were evaluated, we set U = C = 0.5. Gaussian noise was generated with the Matlab function 'random'.

The choice of MAPE values is justified as follows:

- AQY empirical fits have a MAPE of around 70% (Fig. 1 and S1).
- $a_{CDOM}(325)$ has the following validation statistics according to Swan et al. (2013): $R^2 = 0.77$, and model-data slope between 0.54 and 1.51 depending on the validation dataset. Our own assessment, based on the matchups between the $a_{CDOM}(330)$ in the in-situ dataset (Galí et al. 2016) and that retrieved from SeaWiFS data (Swan et al., 2013), returned the following statistics: $R^2 = 0.85$, MAPE = 31%, RMSE = 0.14, mean bias = 2% for daily composites (n = 4), and $R^2 = 0.89$, MAPE = 32%, RMSE = 0.07 and mean bias = -23% for 8-day composites (n = 33), using 5x5 macropixels for matchups in both cases. Although larger datasets would be needed to obtain representative validation statistics in our specific dataset, it may be reasonable to assume that $a_{CDOM}(330)$ retrievals have MAPE = 30% at the scale of 1ºx1º pixels used for global photolysis estimates, because fine-scale spatiotemporal mismatches between in situ data and satellite pixels tend to cancel out over larger scales.

- K_d has MAPE between 15% and 20% (Cao et al. 2014) for the 6 SeaUV spectral bands (320, 340, 380, 412, 443, 490 nm). The MAPE = 30% used here is probably an upper bound.

- Chl typically has $\log_{10}$ root-mean-squared error between 0.16 and 0.25 for in situ matchup data representative of the open ocean environment (Brewin et al. 2016). These values correspond approximately to MAPE between 25% and 40%. Given

that errors tend to cancel out when averaged over the larger 1ºx1º pixels over monthly periods used here, we prescribe MAPE = 30%.

- Broadband PAR estimates at monthly resolution have RMSE = 9.6% (Somayajula et al. 2018) for the combination of SBDART with MODIS Aqua input variables (Table 4, method "SB_M"). For normally distributed (Gaussian) error, this corresponds approximately to a MAPE = 8%. Note also that spectral E_d error in the UV is likely larger than broadband PAR error, but that spectrally-uncorrelated error will partially cancel out when computing spectrally-integrated variables like $k_{p,ML}$. Hence, here we assume MAPE = 10%.

To quantify the uncertainty associated with each variable we calculated the ratio between the reference run (*CDOM_NO3*) and each perturbed run for the ensemble of monthly 1ºx1º pixels. Given that this ratio had a non-normal distribution in many cases (Fig. S3), we report the following non-parametric dispersion metrics in Table S1: the median ratio between the perturbed and the reference run (quantile 0.5), and the quantiles 0.16 and 0.84. These quantiles bracket the 68% central values and correspond, therefore, to ± 1 standard deviation of a Gaussian distribution.

The AQY(λ) caused the largest uncertainty, with perturbed/reference ratios usually between 0.5 and 2 and a non-normal distribution, with a long right tail but a mode < 1. The following largest sources of uncertainty were $K_d(\lambda)$ and $a_{CDOM}(\lambda)$ spectra, whose perturbation caused similar dispersion but larger right skewness in the case of $K_d(\lambda)$. Smaller uncertainty was associated with $E_{d,0^-}(\lambda)$ and Chl, in this order. Therefore, the sensitivity of modeled photolysis rates to the bio-optical relationships used to compute μ_d (eq. S2–10) is small. Finally, note that the uncertainty caused by the combination of perturbed $a_{CDOM}(\lambda)$, $K_d(\lambda)$, $E_{d,0^-}(\lambda)$ and Chl is also non-normally distributed, but smaller than that caused by AQY(λ) alone. This test further justifies the use of 2 alternative AQY(λ) parameterizations in the main article to obtain a more realistic uncertainty assessment. We did not combine perturbations of AQY(λ) with perturbations of the other variables because in our model AQY(λ) is a function of $a_{CDOM}(\lambda)$, such that altering both variables simultaneously might overestimate uncertainty.

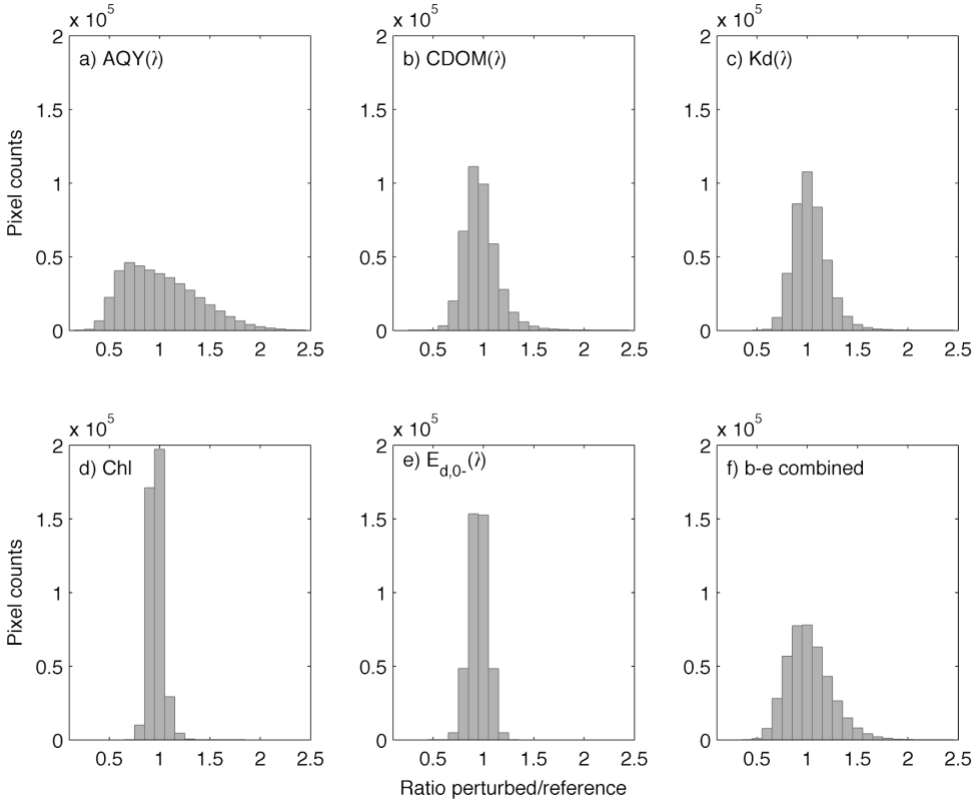

Figure S3*. Summary of the uncertainty assessment based on the addition of gaussian noise (SM3). For each altered variable, we show the histogram of the ratio between the altered and the reference fields of $k_{p,ML}$. Larger spread around 1 indicates larger uncertainty associated with that variable. Selected quantiles are reported in Table S1.*

SM4. Comparison between PAR-driven simplified schemes in global models

The k^{PAR} parameter (eq. 5) and the PAR forcing fields together determine the spatiotemporal changes in sea-surface photolysis in the *K0_SCALED* scheme. In our study we set $k^{PAR} = 0.0128$ m^2 (mol photons)$^{-1}$, the median of 111 globally distributed measurements of $k_{p,0-}$ divided by their corresponding SBDART-derived PAR_{0-} (Galí et al. 2016). This value was chosen to facilitate comparisons between *K0_SCALED* and the models based on AQY spectra from the same dataset but differs largely from those employed in other models.

In Table S2 we compare the value of k^{PAR} across different models, focusing on global studies published after the review of Vézina (2004). Given that in most cases irradiance was expressed in energy units instead of quantum units, we interconverted between them units using a factor of $2.5 \cdot 10^{18}$ quanta s^{-1} W^{-1} (Morel and Smith 1974), which is equivalent to assuming that 100 W/m^2 = 36 mol photons m^{-2} d^{-1}. This conversion factor is

valid only for broadband PAR (400-700 nm) just below the sea surface because of the progressive spectral shift that occurs deeper down the water column.

***Table S1**. Summary of the uncertainty assessment based on the addition of gaussian noise (SM3). For each altered variable, we report the 16%, 50% and 84% quantiles of the ratio between the altered and the reference fields of $k_{p,ML}$. Larger spread around a ratio of 1 indicates larger uncertainty associated with that variable. The bottom row shows the result of simultaneously altering variables b-e. The distributions of the same variables are shown in Fig. S3.*

Altered variable	Prescribed MAPE	Quantile 0.16	Quantile 0.50 (median)	Quantile 0.84
a) AQY(λ)	70%	0.69	1.01	1.45
b) $a_{CDOM}(\lambda)$	30%	0.87	1.00	1.17
c) $K_d(\lambda)$	30%	0.93	1.07	1.24
d) Chl	30%	0.95	1.00	1.07
e) $E_{d,0^-}(\lambda)$	10%	0.91	1.00	1.09
b-e combined	Variable-specific	0.86	1.04	1.28

Vézina (2004) proposed a value of k^{PAR} (named ϕ in their study) of 0.072 m^2 W^{-1} d^{-1}. This value is equivalent to the hourly parameter ϕ = 0.003 m^2 W^{-1} h^{-1} *apparently* used by Lefèvre et al. (2002). We highlight *apparently* because the value reported by Lefèvre et al. (2002) in the text has an order-of-magnitude error. Quoting from that study:

"With onboard experiments in the equatorial Pacific Kieber et al. (1996) found a rate of 0.054 h^{-1} at an average irradiance of 750 W m^{-2} during 4 h for yearday 74 at latitude 0°. With our spectral module, the irradiance calculated between 400 and 460 nm for that day at the sea surface was found to be approximately 25% of the total irradiance. We calculated ϕ = 0.054 / (750·0.25) = 0.003 h^{-1} (W m^{-2})$^{-1}$ so that ϕ, the photo-oxidation rate, varies with depth and season along with the irradiance between 400 and 460 nm. Using this ϕ value on day 74 at latitude 0°, the model calculates a photolysis rate at the sea surface varying from 0.047 h^{-1} (with 90% cloud cover) to 0.067 h^{-1} (with no cloud cover)".

Obviously, $\phi = 0.054 / (750 \cdot 0.25) = 0.0003\ h^{-1}\ (W\ m^{-2})^{-1}$, is tenfold lower than the value given in the text.

The model study of Bopp et al. (2008) used the parameterization proposed by Vézina (2004) and calculated photolysis rates as $P = \lambda^{PAR}_{DMS} \cdot PAR \cdot [DMS]$. In Bopp's model λ^{PAR}_{DMS} was set to 0.05 $m^2\ W^{-1}\ d^{-1}$, and photolysis was forced using total PAR rather than the 25% of total shortwave irradiance, likely leading to overestimation of photolysis rates.

Vogt et al. (2010) followed the parameterization of Bopp et al. (2008) and set their corresponding parameter (named λ^{light}) to the same value, 0.05 $m^2\ W^{-1}\ d^{-1}$. However, Vogt's paper gives confusing information on parameter units. According to their Table 1 the units of λ^{light} are d^{-1}. However, photolysis rates are computed as $P = \lambda^{light} \cdot PAR \cdot [DMS]$ (eq. 4 and eq. 20 of Vogt et al. (2010)), which suggests λ^{light} actually has units of $m^2\ W^{-1}\ d^{-1}$ and the parameterization is therefore identical to that in Bopp et al. (2008).

Belviso et al. (2012) introduced some innovations in the parameterisation of DMS photolysis that remained in subsequent versions of the PISCES model (Masotti et al. 2015) and apparently up to recent CMIP6 simulations (Bock et al. 2021). First, Belviso et al. (2012) computed the PAR dependent photolysis rate constant using a Michaelis-Menten formulation following Archer et al. (2002):

$$\lambda^{PAR}_{DMS} = f3 \cdot PAR/(PAR + h1) \qquad \text{(eq. S13)}$$

where $f3 = 0.25\ d^{-1}$ and $h1 = 5\ W\ m^{-2}$. Second, they added nitrate-dependent modulation of photolysis:

$$\lambda^{NO3}_{DMS} = \max(L^{DMS}_{NO3}, 0.01) \qquad \text{(eq. S14)}$$

$$L^{DMS}_{NO3} = [NO_3] / ([NO_3] + 10\ \mu M) \qquad \text{(eq. S15)}$$

Photolysis rates were finally computed as

$$P = \lambda^{NO3}_{DMS}\ \lambda^{NO3}_{DMS}\ [DMS] \qquad \text{(eq. S16)}$$

As a result, photolysis rate constants in this scheme (the product $\lambda^{NO3}_{DMS}\ \lambda^{NO3}_{DMS}$) cannot exceed $f3 = 0.25\ d^{-1}$, and will be less than half of it wherever nitrate is lower than 10 µM or PAR is lower than 5 $W\ m^{-2}$. This makes us wonder whether the actual expression should be

$$P = (\lambda^{NO3}_{DMS} + \lambda^{NO3}_{DMS})\ [DMS] \qquad \text{(eq. S17)}$$

which would increase sea-surface photolysis rate constants from ~0.25 d^{-1} to ~0.75 d^{-1} for $[NO_3] = 10\ \mu M$, which seems to better represent observations. This parameterization was adopted in subsequent PISCES model versions, possibly up to the PISCES-v2-gas model

employed in the recent CMIP6 exercise (Bock et al. 2021).

In Table S2 we also estimate the maximal mean daily photolysis rates that can be achieved in each model, assuming a mean daily irradiance of 62.5 mol photons m^{-2} d^{-1} just below the sea surface, which is the maximal mean daily value for PAR_{0-} in our monthly climatology computed with SBDART. This value is equivalent to 173 W m^{-2} according to the above conversion factors. One can arrive at a very similar value from simple astronomical calculations. With a mean top-of-atmosphere solar irradiance ("solar constant") of 1368 W m^{-2}, the maximal daily mean shortwave irradiance at the sea surface (latitudes between 80°N and 80°S) would be 447 W m^{-2} during the month of the summer solstice. Note that this value does not consider atmospheric attenuation. Assuming a standard 6% sea-surface reflectance (Kirk 2011), we obtain 420 W m^{-2} just below the sea surface. Given that the PAR wavelengths typically account for 43% of total shortwave irradiance (Kirk 2011), the maximal daily mean PAR irradiance is approximately 181 W m^{-2}, 5% higher than 173 W m^{-2}. This difference can be accounted for by atmospheric attenuation on a very clear day.

Finally, we note that some global model studies were not analyzed here because their descriptions of photolysis parameterizations were not detailed enough (Elliott 2009; Cameron-Smith et al. 2011; Wang et al. 2015, 2018a; b).

***Table S2**. Summary of the values of k^{PAR} used in different models. Bold face is used to highlight k^{PAR} in the original units used in each model. The maximal daily photolysis rates of each model are computed assuming a maximal mean daily PAR irradiance of 62.5 mol photons m^{-2} d^{-1}, approximately equivalent to 173 W m^{-2}.*

Reference	Original name of k^{PAR}	k^{PAR} [m^2 (mol phot.)$^{-1}$]	k^{PAR} [m^2 W^{-1} d^{-1}]	Maximum daily $k_{p,0-}$ [d^{-1}]
Vézina (2004)	ϕ	0.20	**0.072**	7.2
Bopp et al. 2008	λ^{PAR}_{DMS}	0.139	**0.05**	8.65
Vogt et al. (2010)	λ^{light}	0.139	**0.05**	8.65
Belviso et al. 2012	not applicable (see SM4 text)	0.0082	**0.0029**	0.5
This study, *K0_SCALED*	k^{PAR}	**0.0128**	0.0046	0.8
This study, *CDOM_NO3*	not applicable: spectrally resolved model			4.47
Galí et al. (2016)	not applicable: meta-analysis of in situ studies			3.66

SM References

Archer, S. D., F. Gilbert, P. Nightingale, M. Zubkov, a Taylor, G. Smith, and P. Burkill. 2002. Transformation of dimethylsulphoniopropionate to dimethyl sulphide during summer in the North Sea with an examination of key processes via a modelling approach. Deep Sea Res. Part II Top. Stud. Oceanogr. **49**: 3067–3101. doi:10.1016/S0967-0645(02)00072-3

Ayyala Somayajula, S., E. Devred, S. Bélanger, D. Antoine, V. Vellucci, and M. Babin. 2018. Evaluation of sea-surface photosynthetically available radiation algorithms under various sky conditions and solar elevations. Appl. Opt. **57**: 3088. doi:10.1364/AO.57.003088

Belviso, S., I. Masotti, A. Tagliabue, and others. 2012. DMS dynamics in the most oligotrophic subtropical zones of the global ocean. Biogeochemistry **110**: 215–241. doi:10.1007/s10533-011-9648-1

Bock, J., M. Michou, P. Nabat, and others. 2021. Evaluation of ocean dimethylsulfide concentration and emission in CMIP6 models. Biogeosciences **18**: 3823–3860. doi:10.5194/bg-18-3823-2021

Bopp, L., O. Aumont, S. Belviso, and S. Blain. 2008. Modelling the effect of iron fertilization on dimethylsulphide emissions in the Southern Ocean. Deep Sea Res. Part II **55**: 901–912. doi:10.1016/j.dsr2.2007.12.002

Brewin, R. J. W., G. Dall'Olmo, S. Pardo, V. van Dongen-Vogels, and E. S. Boss. 2016. Underway spectrophotometry along the Atlantic Meridional Transect reveals high performance in satellite chlorophyll retrievals. Remote Sens. Environ. **183**: 82–97. doi:10.1016/j.rse.2016.05.005

Bricaud, A., M. Babin, H. Claustre, J. Ras, and F. Tièche. 2010. Light absorption properties and absorption budget of Southeast Pacific waters. J. Geophys. Res. Ocean. **115**: 1–19. doi:10.1029/2009JC005517

Bricaud, A., A. Morel, M. Babin, K. Allali, and H. Claustre. 1998. Variations of light absorption by suspended particles with chlorophyll a concentration in oceanic (case 1) waters : Analysis and implications for bio-optical models Abstract . Spectral absorption coefficients of total particulate matter mg m-3). As pre. J. Geophys. Res. **103**: 31033–31044.

Cameron-Smith, P., S. Elliott, M. Maltrud, D. Erickson, and O. Wingenter. 2011. Changes in dimethyl sulfide oceanic distribution due to climate change. Geophys. Res. Lett. **38**: 1–5. doi:10.1029/2011GL047069

Cao, F., C. G. Fichot, S. B. Hooker, and W. L. Miller. 2014. Improved algorithms for accurate retrieval of UV/visible diffuse attenuation coefficients in optically complex, inshore waters. Remote Sens. Environ. **144**: 11–27. doi:10.1016/j.rse.2014.01.003

Elliott, S. 2009. Dependence of DMS global sea-air flux distribution on transfer velocity and concentration field type. J. Geophys. Res. **114**: G02001. doi:10.1029/2008JG000710

Fichot, C. G., and W. L. Miller. 2010. An approach to quantify depth-resolved marine photochemical fluxes using remote sensing: Application to carbon monoxide (CO) photoproduction. Remote Sens. Environ. **114**: 1363–1377. doi:10.1016/j.rse.2010.01.019

Galí, M., D. J. Kieber, C. Romera-Castillo, and others. 2016. CDOM Sources and Photobleaching Control Quantum Yields for Oceanic DMS Photolysis. Environ. Sci. Technol. **50**: 13361–13370. doi:10.1021/acs.est.6b04278

Kieber, D. J., J. Jiao, R. P. Kiene, and T. S. Bates. 1996. Impact of dimethylsulfide photochemistry on methyl sulfur cycling in the equatorial Pacific Ocean. J. Geophys. Res. **101**: 3715–3722. doi:10.1029/95JC03624

Kirk, J. T. O. 1991. Volume scattering function, average cosines, and the underwater

light field. Limnol. Oceanogr. **36**: 455–467. doi:10.4319/lo.1991.36.3.0455

Kirk, J. T. O. 2011. Light and photosynthesis in aquatic ecosystems, Cambridge.

Laliberté, J., S. Bélanger, and R. Frouin. 2016. Evaluation of satellite-based algorithms to estimate photosynthetically available radiation (PAR) reaching the ocean surface at high northern latitudes. Remote Sens. Environ. **184**: 199–211. doi:10.1016/j.rse.2016.06.014

Lefèvre, M., A. Vézina, M. Levasseur, and J. W. H. Dacey. 2002. A model of dimethylsulfide dynamics for the subtropical North Atlantic. Deep. Res. Part I Oceanogr. Res. Pap. **49**: 2221–2239. doi:10.1016/S0967-0637(02)00121-8

Loisel, H., and A. Morel. 1998. Light Scattering and Chlorophyll Concentration in Case 1 Waters: A Reexamination. Limnol. Oceanogr. **43**: 847–858. doi:10.4319/lo.1998.43.5.0847

Maritorena, S., D. A. Siegel, and A. R. Peterson. 2002. Optimization of a semianalytical ocean color model for global-scale applications. Appl. Opt. **41**: 2705–2714. doi:10.1364/AO.41.002705

Masotti, I., S. Belviso, L. Bopp, A. Tagliabue, and E. Bucciarelli. 2015. Effects of light and phosphorus on summer DMS dynamics in subtropical waters using a global ocean biogeochemical model. Environ. Chem. doi:10.1071/EN14265

Morel, A., B. Gentili, H. Claustre, M. Babin, A. Bricaud, J. Ras, and F. Tièche. 2007. Optical properties of the “clearest” natural waters. Limnol. Oceanogr. **52**: 217–229.

Morel, A., and R. C. Smith. 1974. Relation between total quanta and total energy for aquatic photosynthesis. Limnol. Oceanogr. **19**: 591–600.

Organelli, E., G. Dall’Olmo, R. J. W. Brewin, F. Nencioli, and G. A. Tarran. 2020. Drivers of spectral optical scattering by particles in the upper 500 m of the Atlantic Ocean. Opt. Express **28**: 34147. doi:10.1364/oe.408439

Pérez, G. L., M. Galí, S.-J. Royer, H. Sarmento, J. M. Gasol, C. Marrasé, and R. Simó. 2016. Bio-optical characterization of offshore NW Mediterranean waters: CDOM contribution to the absorption budget and diffuse attenuation of downwelling irradiance. Deep Sea Res. Part I.

Ricchiazzi, P., S. Yang, C. Gautier, and D. Sowle. 1998. SBDART: A Research and Teaching Software Tool for Plane-Parallel Radiative Transfer in the Earth’s Atmosphere. Bull. Am. Meteorol. Soc. **79**: 2101–2114. doi:10.1175/1520-0477(1998)079<2101:SARATS>2.0.CO;2

Swan, C. M., N. B. Nelson, D. A. Siegel, and E. A. Fields. 2013. A model for remote estimation of ultraviolet absorption by chromophoric dissolved organic matter based on the global distribution of spectral slope. Remote Sens. Environ. **136**: 277–285. doi:10.1016/j.rse.2013.05.009

Toole, D. A., D. J. Kieber, R. P. Kiene, D. A. Siegel, and N. B. Nelson. 2003. Photolysis and the dimethylsulfide (DMS) summer paradox in the Sargasso Sea. Limnol. Oceanogr. **48**: 1088–1100. doi:10.4319/lo.2003.48.3.1088

Vézina, A. F. 2004. Ecosystem modelling of the cycling of marine dimethylsulfide: A review of current approaches and of the potential for extrapolation to global scales. Can. J. Fish. Aquat. Sci. **61**: 845–856. doi:10.1139/F04-025

Vogt, M., S. M. Vallina, E. T. Buitenhuis, L. Bopp, and C. Le Quéré. 2010. Simulating dimethylsulphide seasonality with the Dynamic Green Ocean Model PlankTOM5. J. Geophys. Res. **115**: 1–21. doi:10.1029/2009JC005529

Wang, S., S. Elliott, M. Maltrud, and P. Cameron-Smith. 2015. Influence of explicit Phaeocystis parameterizations on the global distribution of marine dimethyl sulfide. J. Geophys. Res. Biogeosciences **120**. doi:10.1002/2015JG003017

Wang, S., M. Maltrud, S. Burrows, S. Elliott, and P. C. Smith. 2018a. Impacts of shifts in phytoplankton community on clouds and climate via the sulfur cycle. Global Biogeochem. Cycles **32**: 1005–1026. doi:10.1029/2017GB005862

Wang, S., M. Maltrud, S. Elliott, P. Cameron-Smith, and A. Jonko. 2018b. Influence of dimethyl sulfide on the carbon cycle and biological production. Biogeochemistry **138**: 49–68. doi:10.1007/s10533-018-0430-5

Zhu, Y., and D. J. Kieber. 2020. Global Model for Depth-Dependent Carbonyl Photochemical Production Rates in Seawater. Global Biogeochem. Cycles **34**: e2019GB006431. doi:10.1029/2019GB006431